MATERIALS SCIENCE

Flexible artificial Si-In-Zn-O/ion gel synapse and its application to sensory-neuromorphic system for sign language translation

Seyong Oh[1†], Jeong-Ick Cho[1†], Byeong Hyeon Lee[2†], Seunghwan Seo[1], Ju-Hee Lee[1], Hyongsuk Choo[1], Keun Heo[3], Sang Yeol Lee[4]*, Jin-Hong Park[1,5]*

We propose a flexible artificial synapse based on a silicon-indium-zinc-oxide (SIZO)/ion gel hybrid structure directly fabricated on a polyimide substrate, where the channel conductance is effectively modulated via ion movement in the ion gel. This synaptic operation is possible because of the low-temperature deposition process of the SIZO layer (<150°C) and the surface roughness improvement of the poly(4-vinylphenol) buffer layer (12.29→1.81 nm). The flexible synaptic device exhibits extremely stable synaptic performance under high mechanical (bending 1500 times with a radius of 5 mm) and electrical stress (application of voltage pulses 10^4 times) without any degradation. Last, a sensory-neuromorphic system for sign language translation, which consists of stretchable resistive sensors and flexible artificial synapses, is designed and successfully evaluated via training and recognition simulation using hand sign patterns obtained by stretchable sensors (maximum recognition rate, 99.4%).

INTRODUCTION

Because Internet of Things (IoT) technologies are being used by not only industries but also individuals, there has been a rapid increase in the demand for portable smart electronic devices that can be connected to the data cloud networks anywhere and anytime (*1*–*3*). In particular, flexible electronics have recently attracted notable attention as future technologies related to robotics and smart health care systems because of their universal applicability and mechanical flexibility (*4*–*7*). In recent years, there have been many efforts to implement flexible electronic devices using various materials, such as organic thin films (*8*–*10*), two-dimensional (2D) materials (*11*–*13*), and amorphous oxide semiconductors (AOSs) (*14*–*16*). Among them, AOSs have shown good potential for flexible electronics in terms of fabrication process, such as low cost, high reliability, and low-temperature processing (*17*, *18*). Choi *et al.* (*19*) reported a flexible silicon-indium-zinc-oxide (SIZO) thin-film transistor (TFT) with good mechanical stability at high strain. The SIZO-TFT was fabricated on a flexible polyimide (PI) substrate at 150°C. Sim *et al.* (*20*) demonstrated multifunctional stretchable human-machine interface (HMI) devices using sol-gel-on-polymer-processed IZO semiconductor nanomembranes. The HMI devices can be easily worn by humans and can also be implemented as prosthetic skin for robotics. Cantatore and co-workers (*21*) implemented a flexible electrocardiogram (ECG) patch on foil with self-aligned indium-gallium-zinc-oxide TFTs. The flexible ECG patch could amplify the measured analog ECG signals and convert them to a digital output for biomedical analysis.

Meanwhile, the demand for future artificial intelligence systems has led to an expansion in the research scope of flexible electronics to neuromorphic devices. Most of the relevant research has focused on the development of synaptic devices, which are the most important components of artificial neural networks (ANNs) for neuromorphic computing technology. Recently, various flexible synaptic devices have been reported (*22*–*25*). Shim *et al.* (*26*) reported a stretchable synaptic transistor based on elastomeric electronic materials, where its synaptic characteristics were retained even when stretched to 150%. Ham *et al.* (*27*) fabricated a 1D fiber-shaped wearable synapse based on a ferroelectric organic transistor, which exhibited excellent reliability under 6000 repeated input stimuli and mechanical bending stress. Zhao *et al.* (*28*) implemented an ionic polymer–based flexible synapse, where its synaptic performance was sustained even when bent to 360° and under 10^4 pulse cycles.

Interesting studies on flexible synaptic devices have been recently reported, where a simple neural system consisting of artificial synapses and sensors was demonstrated (*29*–*33*). This neural system was referred to as a sensory-neuromorphic system; the system mimicked the nervous system, was capable of the transduction and processing of signals sensed in real time, and afforded biological benefits such as fault tolerance and low power consumption. Thus far, many studies on sensory-neuromorphic systems have been conducted. For instance, in 2017, a tactile perception system consisting of organic-based synaptic transistors and pressure sensors was proposed by Zang *et al.* (*31*). Kim *et al.* (*32*), in 2018, implemented an artificial afferent nerve system composed of flexible synaptic transistors and pressure sensors, highlighting that the synaptic transistor can be used to interface with biological efferent nerves to form a complete monosynaptic reflex arc. In 2020, Kim *et al.* (*33*) reported a tactile sensory-neuromorphic system based on tactile sensors and carbon nanotube (CNT)–based synapses. They highlighted the potential to further improve the technologies used in cyborg and neuromorphic system by endowing supramodal perceptual capabilities. Although the proof of feasibility of the flexible synaptic devices and sensor-embedded synapses was performed, more studies on synaptic performance evaluation are still required

[1]Department of Electrical and Computer Engineering, Sungkyunkwan University, Suwon 16419, Korea. [2]Department of Microdevice Engineering, Korea University, Seoul 02841, Korea. [3]Department of Semiconductor Science and Technology, Chonbuk National University, Jeonju 54896, Korea. [4]Department of Electronic Engineering, Gachon University, Seongnam 13306, Korea. [5]SKKU Advanced Institute of Nano Technology (SAINT), Sungkyunkwan University, Suwon 16419, Korea.
*Corresponding author. Email: sylee2020@gachon.ac.kr (S.Y.L.); jhpark9@skku.edu (J.-H.P.)
†These authors contributed equally to this work.

for the application to complex ANNs. Moreover, there have been few studies involving an entire system-level performance investigation via the training and recognition tasks using data obtained by the sensors thoroughly.

Here, we report a flexible synaptic device based on a SIZO/ion gel hybrid structure that maintains a highly stable performance under mechanical and electrical stress. The SIZO semiconducting channel was successfully formed on a poly(4-vinylphenol) (PVP)–coated flexible PI substrate via the low-temperature SIZO deposition process, and the surface roughness was improved by the PVP buffer layer. To evaluate the performance stability with mechanical flexibility and durability, we investigate the static and dynamic characteristics of the synaptic device with respect to the bending radius and cycle. Then, the optimization of the dynamic range (G_{max}/G_{min}) and asymmetricity (AS) of long-term potentiation/depression (LTP/D) is conducted via pulse engineering, followed by an examination of the relevant cycle-to-cycle variations. Last, we conduct training and recognition tasks for sign language patterns obtained from prefabricated stretchable sensors and evaluate the performance of flexible sensory-neuromorphic systems.

RESULTS

Flexible synaptic device based on the SIZO/ion gel hybrid structure

A biological synapse is located at the connection between two adjacent neurons, where the strength of the connected neural pathways is called the "synaptic weight." The synaptic weight is determined by the storage of information, and it is strengthened or weakened by the release of neurotransmitters (*34*). To mimic the configuration and functions of the biological synapse, we fabricated an artificial synapse with a SIZO/ion gel hybrid structure, as shown in the schematic images in Fig. 1A. Here, the SIZO semiconducting channel is located between two Au electrodes, which denote presynaptic (T_{pre}) and postsynaptic terminals (T_{post}), respectively. When a presynaptic voltage (V_{pre}) is applied to T_{pre}, a postsynaptic current (I_{post}) flows from T_{pre} to T_{post}; the postsynaptic conductance (G_{post}) is determined using the following equation: $G_{post} = I_{post}/V_{pre}$. Moreover, G_{post} is modulated by the movement of mobile ions in the ion gel via the weight control voltage (V_{WC}). Figure 1B shows the flexible synaptic device array with a size of 3 × 3, which was fabricated directly on the PVP-coated PI substrate, and the optical microscopy (OM) image of the magnified single device. This was possible because of the low-temperature deposition process of the SIZO channel layer (<150°C) and the minimized surface roughness by the PVP buffer layer. We introduced PVP buffer layers of 1 weight % (wt %) and 3 wt % between the SIZO channel and the PI substrate, followed by an investigation of the surface roughness via atomic force microscopy (AFM). As seen in the AFM images in Fig. 1C, the surface roughness was slightly improved after introducing the PVP buffer layer of 1 wt % and further improved with a 3 wt % PVP layer. We calculated the root mean square of the microscopic peaks and valleys measured at the surfaces ($RMS_{roughness}$), as shown in Fig. 1D. The $RMS_{roughness}$ value was improved significantly from 12.29 to 1.81 nm, which clearly indicates that the PVP buffer layer significantly contributed to the direct deposition of the SIZO channel layer on the PI substrate. This improvement in the surface roughness is attributed to the high viscosity of the PVP solution (*35*). We then investigated the static postsynaptic current versus weight control voltage (I_{post}-V_{WC}) characteristics of the synaptic device (Fig. 1E). Compared with the device without the PVP layer, the 3 wt % PVP–inserted device exhibited a I_{post}-V_{WC} characteristic curve with relatively high on current, high on/off current ratio, and large memory window, which may be due to the improvement in the surface roughness. The decreased surface roughness improves the quality of the PVP-SIZO interface, which, in turn, suppresses interfacial scattering and trapping. This is expected to improve the I_{post}-V_{WC} characteristics. For this measurement, we swept the V_{WC} from −20 to +20 V (first sweep: forward direction) and from +20 to −20 V (second sweep: reverse direction) and applied a constant V_{pre} of 1 V. The memory window represents the difference between the threshold voltage (V_{th}) values of the first and second curves (ΔV_{th}).

We then investigated the conductance response of the flexible synaptic device according to the continuous V_{WC} pulses (Fig. 1F), where the pulse width and frequency were fixed at 50 ms and 5 Hz, respectively. To monitor the conductance change, a V_{pre} value of 1 V was applied to T_{pre}. Because 100 positive V_{WC} pulses of +5 V were applied to the weight control terminal (T_{WC}), G_{post} increased linearly from 0.6 to 27.8 nS. It also decreased gradually to the initial conductance level after applying 100 negative V_{WC} pulses of −5 V. This result is quite impressive because an artificial synapse should have a multistate that can be modulated linearly and reproducibly for the successful implementation of a hardware neural network (HW-NN) (*36*–*41*). This conductance response originates from the gradual ion movement inside the ion gel according to V_{WC} (Fig. 1G and fig. S1). When a positive V_{WC} is applied, the positive ions ($[EMIM]^+$) in the ion gel are pushed away from T_{WC} to the SIZO channel, and the negative ions ($[TFSI]^-$) are simultaneously pulled to T_{WC} (see SIZO/ion gel interface). As indicated by the energy band diagrams in Fig. 1G, the positive ions induce the accumulation of electron carriers in the SIZO channel region, thereby increasing the surface potential. This increases the electron injection probability at the postsynaptic terminal/SIZO junction, leading to the conductance potentiation phenomenon. On the other hand, when a negative V_{WC} is applied, the positive ions are dragged to T_{WC}, and the negative ions move to the SIZO channel region at the same time. Similarly, as indicated by the energy band diagrams in Fig. 1H, the negative ions induce the accumulation of hole carriers in the SIZO channel, leading to a decrease in the surface potential. Thus, the probability of electron injection at the presynaptic terminal/SIZO junction decreases, leading to the conductance depression phenomenon (see also fig. S1). The ions in the ion gel move toward the SIZO surface region because of the positive voltage pulses and form a temporary electric double layer (EDL) at the interface between the ion gel and the SIZO (*42*, *43*). When applying the negative voltage pulses, the accumulated ions diffuse back into the ion gel medium, gradually decomposing the EDL (*43*). In the case of the proposed device, when a positive V_{WC} is applied (i.e., $V_{WC} > 5$ V), the ions accumulate near the interface and are also adsorbed into the existing defects in the SIZO channel region. The ions that form the EDL rapidly diffuse into the ion gel under a negative V_{WC}; however, the adsorbed ions are expected to be removed slowly, which likely causes the short-term and long-term synaptic plasticity (see also fig. S2 for short-term synaptic plasticity).

Mechanical flexibility and durability of SIZO/ion gel synaptic device

In flexible neuromorphic electronics, it is important to maintain stable electrical characteristics under mechanical stresses that occur

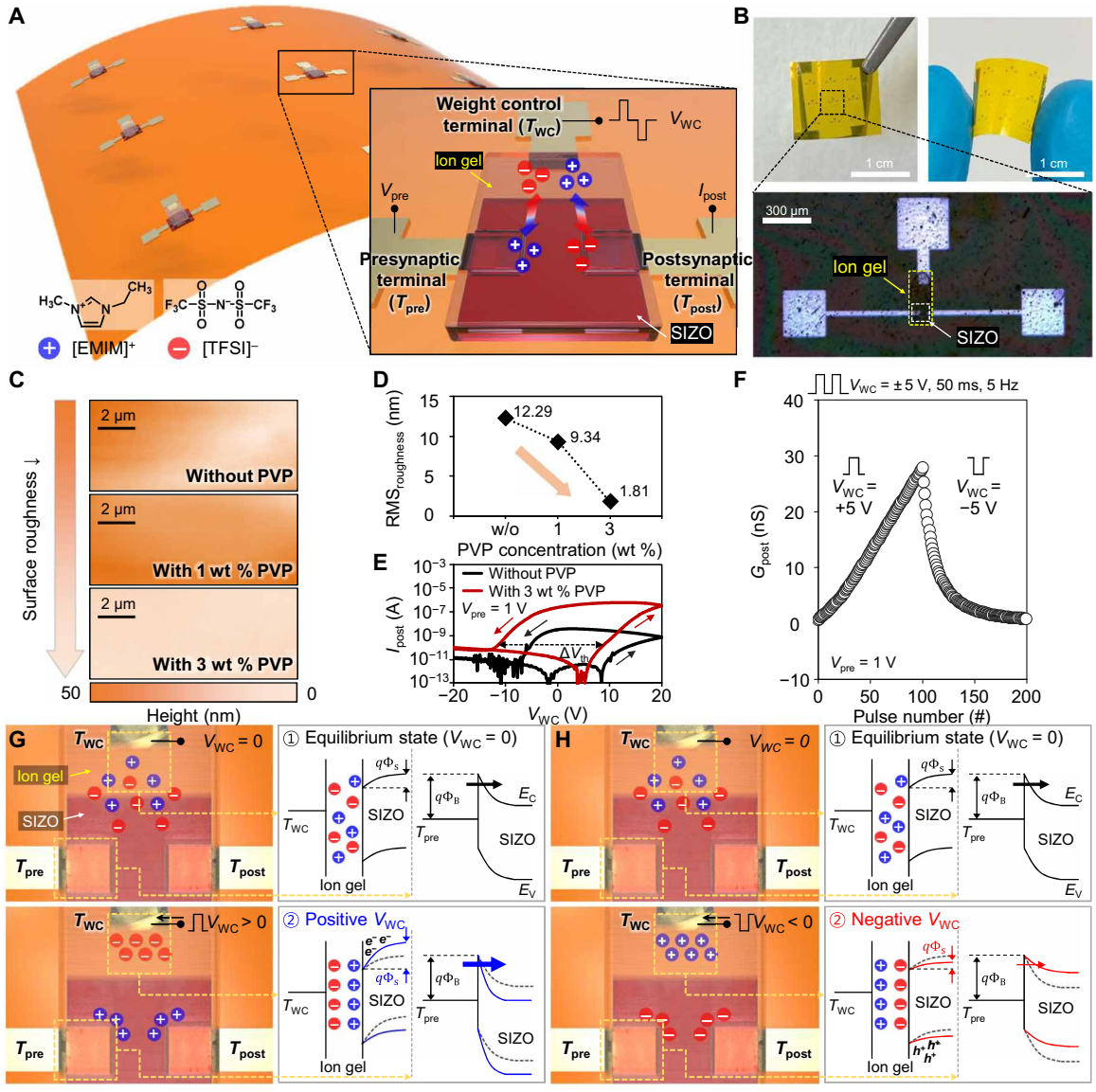

Fig. 1. Flexible synaptic device based on the SIZO/ion gel hybrid structure. (**A**) Schematic images of the flexible synaptic device based on a SIZO/ion gel hybrid structure. (**B**) Flexible synaptic device array with a size of 3 × 3, which was fabricated directly on the PVP-coated PI substrate and the OM image of the magnified single device. (**C**) AFM mapping images of the SIZO surface without/with the insertion of the PVP buffer layer. (**D**) Calculated $RMS_{roughness}$ values with respect to the PVP concentration. (**E**) Static I_{post}-V_{WC} characteristic of the synaptic device without PVP buffer layer (black) and 3 wt % PVP buffer layer (wine). (**F**) Conductance response of the flexible synaptic device according to the continuous V_{WC} pulses, where the pulse width and frequency were fixed as 50 ms and 5 Hz, respectively. (**G** and **H**) Weight update mechanism of the SIZO/ion gel synaptic device when the positive (G) and negative V_{WC} (H) was applied, respectively. The left panels are illustrations of the ion movement in the SIZO/ion gel synaptic device, and the right panels are the energy band diagrams according to the applied V_{WC} (photo credit: Jeong-Ick Cho, Sungkyunkwan University).

when the synaptic device is stretched or bent. In particular, robustness against tensile stress by bending is a key factor for the application of synaptic devices in future flexible electronics such as wearable computing, soft robotics, and neuroprosthetics (*44*). In this section, to demonstrate the mechanical flexibility and durability of the SIZO/ion gel–based artificial synapse, we investigated the synaptic performance stability with respect to the bending radius and cycle. For the bending flexibility test, a synaptic device array fabricated on a PI film with a size of 2 × 2 cm^2 was attached to the arch-shaped metal bars with radii of 30, 10, or 5 mm using scotch tape, as shown in Fig. 2A and fig. S3A. The static I_{post}-V_{WC} characteristics were then analyzed with respect to the bending radius (Fig. 2B). The V_{WC} was swept from −20 to +20 V (first sweep: forward direction) and from +20 to −20 V (second sweep: reverse direction), where a constant V_{pre} of 1 V was applied to T_{pre}. In all the bending cases, the I_{post}-V_{WC} characteristics were not changed significantly. As shown in the top panel of Fig. 2D, ΔV_{th} barely changed at approximately 20 V, even when bent to a radius of 5 mm. The relative standard deviation (RSD) was only 1.1%, indicating excellent stability for mechanical flexibility (RSD = SD/mean). We then investigated the dynamic characteristics of synaptic devices with respect to the bending radius. For each radius, the response of G_{post} to 100 positive and 100

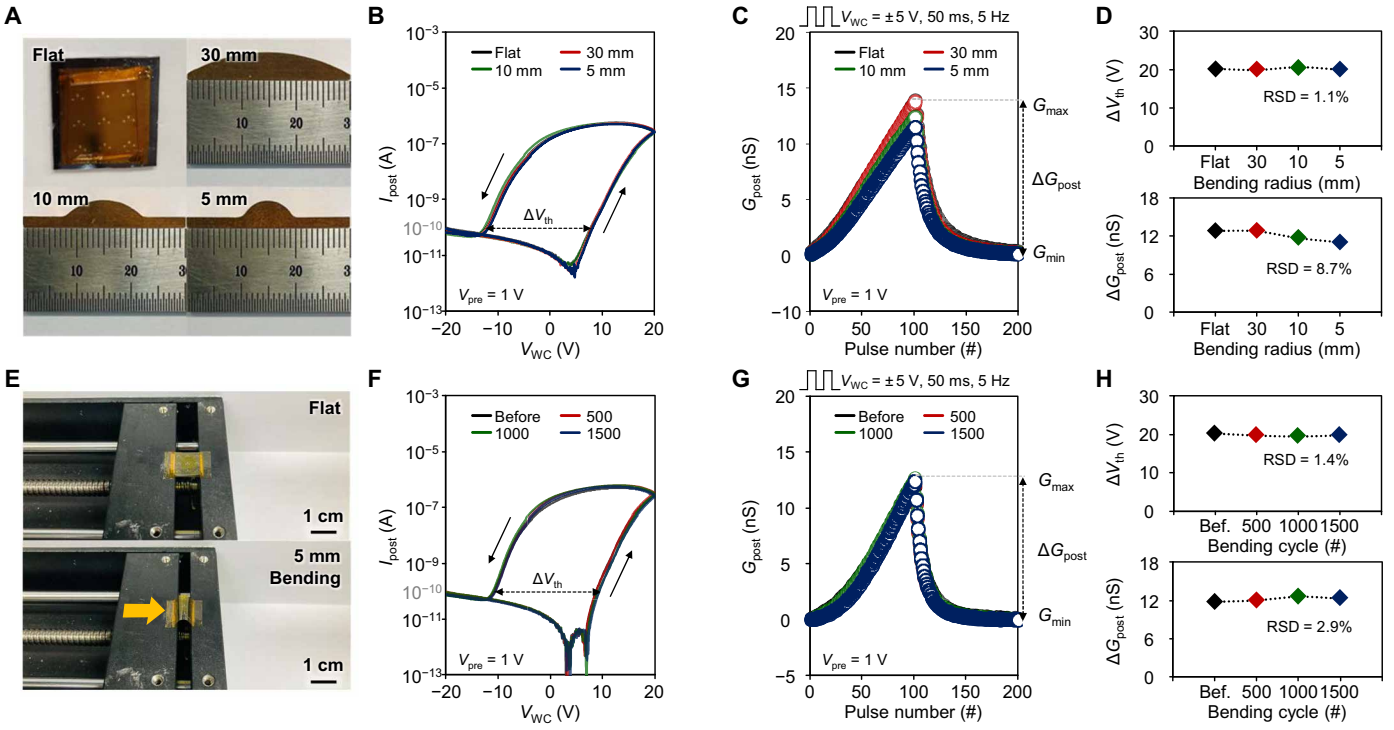

Fig. 2. Mechanical flexibility and durability of the SIZO/ion gel synaptic device. (**A**) Measurement images for mechanical flexibility of the SIZO/ion gel synaptic device. The flexible synapse was attached to the arch-shaped metal bars with a radius of 30, 10, or 5 mm using scotch tape. (**B** and **C**) Static I_{post}-V_{WC} and dynamic LTP/D characteristics with respect to the bending radius. (**D**) Extracted ΔV_{th} (top panel) and ΔG_{post} (bottom panel) and their RSDs with respect to the bending radius. (**E**) Measurement images for mechanical durability of the SIZO/ion gel synaptic device. The side parts of the PI film including the synaptic device array were attached to the bending machine using scotch tape, and then, we operated the bending machine to apply tensile stress to the device repeatedly 500, 1000, and 1500 times. (**F** and **G**) Static I_{post}-V_{WC} and dynamic LTP/D characteristics of the synaptic device with regard to the bending cycle. (**H**) Extracted ΔV_{th} (top panel) and ΔG_{post} (bottom panel) and their RSDs with regard to the bending cycle (photo credit: Jeong-Ick Cho, Sungkyunkwan University).

negative V_{WC} voltage pulses was monitored, where the magnitude, width, and frequency of the pulse were 5 V, 50 ms, and 5 Hz, respectively. As shown in Fig. 2C, the measured LTP/D characteristic curves were very similar to each other in all bending radius tests. Although the extracted ΔG_{post} (= G_{max} − G_{min}) slightly changed from 13.5 to 11.25 nS as the device was bent to 5 mm, the RSD for the bending radius was still as small as 8.7% (bottom panel of Fig. 2D). The stable device flexibility is attributed to (i) the excellent flexibility of the SIZO (*19*, *45*) and ion gel (*46*, *47*) layers and (ii) the extremely small bending strain (ε) of 0.26%, originating from the significantly low device thickness (fig. S4).

We also examined the mechanical durability of the bending cycle with the SIZO/ion gel artificial synapse, where the bending radius was set to 5 mm and the bending speed was controlled using a commercial bending machine (ECOPIA, step motor controller, SMC 100). As shown in Fig. 2E and fig. S3B, the side parts of the PI film, including the synaptic device array, were attached to the bending machine using scotch tape, and the bending machine then repeatedly applied tensile stress to the device. After 500, 1000, and 1500 repeated bending cycles, we placed the device sample onto the flat substrate and analyzed the I_{post}-V_{WC} and LTP/D characteristics, as shown in Fig. 2 (B and C). In the static characteristic analysis, the synaptic device exhibited very stable I_{post}-V_{WC} characteristics with regard to the bending cycle; the V_{th} values of the first and second curves were maintained even after 1500 bending cycles (Fig. 2F). The calculated ΔV_{th} values were constant at approximately 20 V, and their RSD was only 1.4%, indicating that the synaptic device had excellent durability against the bending cycle (upper panel of Fig. 2H). Moreover, the device exhibited very stable LTP/D characteristics, where the conductance modulation by the voltage pulses was perfectly repeated even for 1500 bending cycles (Fig. 2G). The extracted ΔG_{post} values showed little fluctuation, but their RSD was only as small as 2.9% (bottom panel of Fig. 2H). In addition, we conducted a performance benchmark in comparison with other studies on the AOS-based flexible synapses (table S1). Our device showed relatively high flexibility (bending radius of 5 mm) and high durability (bending cycle of 1.5×10^3).

Controllability and electrical stability of dynamic characteristics

The performance of an HW-NN is strongly dependent on the dynamic characteristics of the synaptic devices composing the network. In particular, G_{max}/G_{min} and AS of the LTP/D characteristics are the most important factors that affect the learning accuracy of the HW-NN (*48*). Thus, it is important to investigate the controllability of synaptic weight modulation and to determine the optimized condition of the weight control signal (V_{WC} in this study) for achieving high G_{max}/G_{min} and low AS for a high learning accuracy. To evaluate the weight modulation ability of the device and investigate the optimal pulse condition, we monitored G_{post} by applying to T_{WC} 100 potentiating and 100 depressing pulses with various pulse amplitude and width conditions (Fig. 3A). We applied V_{WC} pulses,

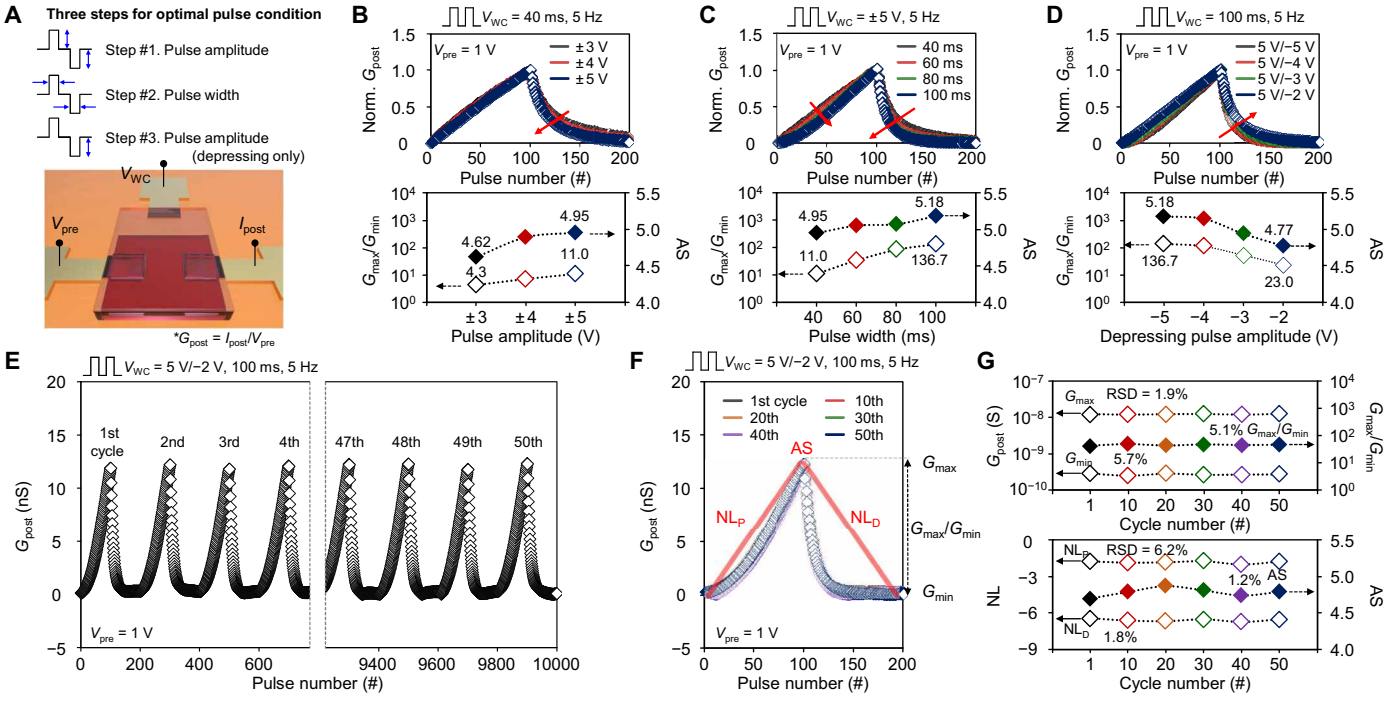

Fig. 3. Controllability and electrical stability of dynamic characteristics. (**A**) Schematic illustration of the SIZO/ion gel synaptic device showing an application of the V_{pre} and V_{WC}, where the V_{WC} was varied according to three steps: step #1, the potentiating and depressing pulse amplitude variations from ±3 to ±5 V; step #2, the pulse width variations from 40 to 100 ms; and step #3, the depressing pulse amplitude variations from −5 to −2 V. (**B** to **D**) Normalized LTP/D characteristic curves according to the pulse number (top panel) and the extracted G_{max}/G_{min} and AS from the curves (bottom panel) corresponding to steps #1 to #3. (**E**) Electrical stability analysis of the dynamic characteristics with the optimal pulse condition (V_{WC} = +5/−2 V, 100 ms, 5 Hz). For the cycle test, a set of V_{WC} pulses consisting of 100 potentiating and 100 depressing pulses was applied to T_{WC} repeatedly 50 times (a total of 10,000 pulses). (**F**) Extracted LTP/D characteristic curves for the first cycle and every 10th cycle from 10th to 50th. (**G**) Extracted G_{max}/G_{min} and AS from the six LTP/D characteristic curves.

whose potentiating and depressing pulse amplitudes varied from ±3 to ±5 V (step no. 1), where the pulse width and frequency were set to 40 ms and 5 Hz, respectively. To visualize the weight modulation trends in the LTP/D characteristic curves, we normalized G_{post} ranging from 0 to 1 (top panel of Fig. 3B). As the pulse amplitude increased from ±3 to ±5 V, the LTP region was maintained, but G_{post} in the LTD region decreased rapidly. To investigate the conductance modulation quantitatively, we extracted G_{max}/G_{min} and AS from the LTP/D characteristic curves (bottom panel of Fig. 3B). Here, G_{max}/G_{min} is the ratio of the maximum and minimum conductance values, and AS is the difference between the nonlinearities in the LTP and LTD regions ($NL_P - NL_D$) (see the detailed nonlinearity extraction method in fig. S5). When a V_{WC} value of ±3 V was applied to the device, G_{max}/G_{min} was too low (4.3), which was not sufficient for the minimum requirement of the dynamic range (>10) for learning. As the pulse amplitude was increased to ±5 V, G_{max}/G_{min} also increased to 11.0, which was slightly higher than the minimum requirement, but it was still too low to achieve a high learning accuracy. Meanwhile, AS degraded from 4.62 to 4.95 as the pulse amplitude increased from ±3 to ±5 V. This result indicates that G_{max}/G_{min} and AS have a trade-off relationship and can be controlled by adjusting the pulse energy applied to T_{WC}. To further improve G_{max}/G_{min}, we adjusted the pulse width of V_{WC} (step no. 2) while maintaining the pulse amplitude and frequency at 5 and 5 Hz, respectively (Fig. 3C). Because the pulse width was varied from 40 to 100 ms, the LTP/D characteristic became more nonlinear, and the characteristic curve in the LTD region changed significantly. G_{max}/G_{min} markedly increased from 11.0 to 136.7, but AS degraded significantly from 4.95 to 5.18. Although G_{max}/G_{min} was sufficiently high for learning, AS was too high, which could significantly degrade the learning accuracy of the HW-NN. The learning accuracy with respect to the pulse condition is presented in fig. S6. A detailed description of the used datasets and the designed neural network is provided in the following section (Fig. 4). As a final step, we adjusted only the amplitude of the depressing pulse (step #3) after fixing the potentiating pulse to 5 V to improve AS and simultaneously secure a reasonable G_{max}/G_{min} value (Fig. 3D). The pulse width and frequency were fixed at 100 ms and 5 Hz, respectively. As the amplitude of the depressing pulse was varied from −5 to −2 V, the linearity of the LTP/D characteristic curve recovered slightly. In addition, AS was significantly improved from 5.18 to 4.77, which is expected to be a desirable pulse condition for achieving a very high learning accuracy of the HW-NN. Furthermore, we extracted the effective number of conductance states between G_{max} and G_{min} (NS_{eff}) from the LTP/D characteristic curves in Fig. 3D (see fig. S7). In the cases of 5 and −2 V pulses, 99 and 87% of the total conductance states were effectively accessible, which indicated that our synaptic device had a sufficient number of conductance states between G_{max} and G_{min}. The high operating voltage pulses are expected to be sufficiently reduced by (i) scaling down the device dimensions, (ii) adjusting the ion gel composition of the weight control layer (WCL), or (iii) replacing the WCL itself with ferroelectric materials including polyvinylidene difluoride, lead-zirconate-titanate, and hafnium zirconium oxide (HZO).

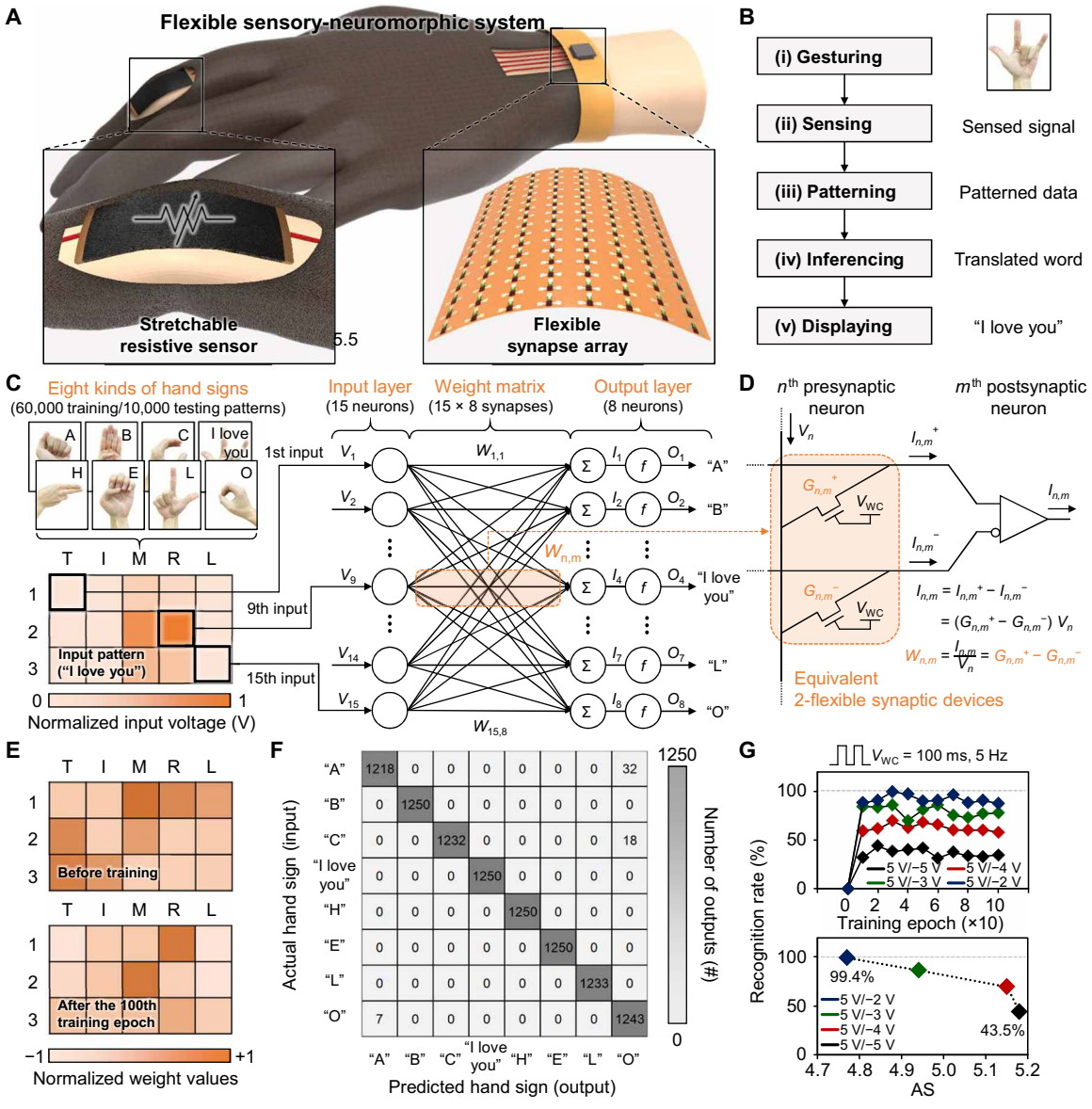

Fig. 4. Sensory-neuromorphic systems for sign language translation. (**A**) Schematic illustration of the designed sensory-neuromorphic system for sign language translation consisting of stretchable resistive sensors and flexible artificial synapses. (**B**) Translation process via the designed sensory-neuromorphic system. Here, we assumed that a user wore a wearable glove on which a flexible sensory-neuromorphic system was embedded for communication with a nondeaf person. (**C**) Designed single-layer ANN with a size of 15 × 8 for the training and recognition simulation with respect to eight disparate hand signs of "A," "B," "C," "I love you," "H," "E," "L," and "O," where "T," "I," "M," "R," and "L" are the thumb, index finger, middle finger, ring finger, and little finger, respectively. Rows "1," "2," and "3" of the input image pattern refer to the distal interphalangeal joints, proximal interphalangeal joints, and metacarpophalangeal joints, respectively (see more detailed information in fig. S10). (**D**) Synaptic weight representation expressed by the conductance difference of two equivalent synaptic devices. (**E**) Mapping images of the normalized synaptic weights for the "I love you" hand sign before training and after finishing the 100th training epoch. (**F**) Confusion matrix between actual (input) and predicted (output) hand signs after the 100th training epoch. (**G**) Recognition rate according to the number of training epochs for the hand sign patterns with respect to the depressing pulse amplitude from −5 to −2 V.

We then investigated the electrical stability of the dynamic characteristics of the synaptic devices with the optimal pulse conditions (V_{WC} = +5/−2 V, 100 ms, 5 Hz). For the cycle test, a set of V_{WC} pulses consisting of 100 potentiating and 100 depressing pulses were applied to T_{WC} 50 times (a total of 10,000 pulses). As shown in Fig. 3E, the LTP/D characteristics of the flexible SIZO/ion gel synaptic device were maintained even after the 50 cycles without any significant degradation, exhibiting high stability under repeated electrical stress. We also extracted the LTP/D characteristic curve for the first cycle and every 10th cycle from 10th to 50th (Fig. 3F). The selected six LTP/D curves showed very similar curve shape, which indicates that our synaptic device could maintain its initial dynamic characteristics even after numerous weight update events for learning. To evaluate its electrical stability more precisely, we extracted G_{max}/G_{min} and AS from the six LTP/D characteristic curves (Fig. 3G). The obtained G_{max} and G_{min} values for 50 cycles remained constant at approximately 12.1 and 0.3 nS, respectively, and consequently, G_{max}/G_{min} was also maintained at approximately 44.8. Because

of their high stability for the cycle, the RSD values of G_{max}, G_{min}, and G_{max}/G_{min} were also as small as 1.9, 5.7, and 5.1%, respectively (top panel of Fig. 3G). Moreover, the nonlinearities of the LTP and LTD curves (NL_P and NL_D) for 50 cycles did not change from their initial values of −1.83 and − 6.61, respectively, and the calculated AS value also showed no degradation at approximately 4.78 against the cycle test. The RSDs of NL_P and NL_D were 6.2 and 1.8%, respectively, and, in particular, that of AS was extremely as small as 1.2% (bottom panel of Fig. 3G). On the basis of the results, we confirmed that the dynamic characteristics of the synaptic devices had a very high stability for electrical stress. In addition, we investigated the reading and writing energy consumption of the synaptic device under potentiation/depression pulse conditions via measurements between T_{pre} and T_{post} and between T_{WC} and T_{post} (see fig. S8).

Sensory-neuromorphic systems for sign language translation

Last, we designed a sensory-neuromorphic system for sign language translation, consisting of stretchable resistive sensors and flexible artificial synapses (Fig. 4A). According to the World Federation of the Deaf, people who are hearing impaired and thereby use sign language as a first "language" account for almost 1% of the world's population and have serious difficulty in communicating with normal people because of the deficiency in terms of language translation system (*49*). Therefore, it is essential to conduct research on the wearable sign language translation system that helps deaf people to communicate with nondeaf people without any delay or obstacles by providing direct and real-time sign language translation. The translation process via the designed sensory-neuromorphic system is as follows (Fig. 4B): (i) gesturing a certain word using sign language ("I love you" in this example), (ii) sensing the hand sign using stretchable sensors attached on each finger joint region, (iii) patterning (filtering, digitizing, and sampling, etc.) the sensed signals as a voltage form, (iv) inferencing the patterned data via a pretrained flexible synapse array, and (v) displaying the translated word on the screen or speaking it as a vocal sound (*50*). Here, we assumed that a user wore a wearable glove on which a flexible sensory-neuromorphic system was embedded for communication with a nondeaf person.

To evaluate the performance of the proposed sensory-neuromorphic system quantitatively, we theoretically constructed a single-layer ANN with a size of 15 × 8 and conducted training and recognition simulation for eight disparate hand signs of "A," "B," "C," "I love you," "H," "E," "L," and "O" (Fig. 4C). The somewhat small size of the ANN is attributed to the limited number of finger joints (only 15 joints), and it can be expanded further to a larger network by adopting a sensor array onto the joints (*51*–*54*). For the simulation, we prepared 60,000 training and 10,000 testing patterns consisting of eight types of hand signs, where each hand sign pattern has a size of 3 × 5 (the detailed sensing and patterning process is shown in figs. S9 to S11). The training process was as follows: The 15 voltage values in the hand sign pattern are applied one-to-one to the 15 input neurons as input voltages (V_1 to V_{15}), and they were then transformed to the output currents (I_1–I_8) via the matrix-vector summation with a synaptic weight matrix ($W_{1,1}$–$W_{15,8}$). Here, synaptic weights can be expressed by the conductance difference between two equivalent synaptic devices, because the conductance of the hardware synaptic device is always positive, unlike that of the synapses in software with both positive and negative values (Fig. 4D) (*55*). Therefore, to map the synaptic weights of the designed fully connected HW-NN, a synaptic array of at least 15 × 8 × 2 is required. Next, the output values (O_1 to O_8) are calculated using the softmax activation function [$O_m = f(I_m)$], and they are further compared to the label value of the output neuron (k_1–k_8) to determine the sign of the weight update [sgn(ΔW)]. Last, all weight values in the synaptic weight matrix are updated according to the determined signs (see Materials and Methods for details). We repeated this training process with 60,000 sets of training data and calculated the recognition rate with 10,000 sets of testing data every 60,000th training step (one training epoch) for 100 training epochs.

As shown in Fig. 4E, the mapping image of the normalized synaptic weights for the "I love you" hand sign had an uncertain shape before training, and the values were randomly distributed from −1 to +1. After finishing the 100th training epoch, the mapping image presented a specific pattern, which indicates that the ANN was well trained for the input hand signs. Here, weight mapping was conducted using a pattern recognition simulator that could monitor the synaptic weights at each training task step. The confusion matrix between the actual (input) and predicted (output) hand signs also showed that the ANN was trained almost perfectly after the 100th training epoch (Fig. 4F). Although the worst confusion case happened between the signs "A" and "O," the sensitivity of each sign was still as high as 97.4 and 99.4%, respectively. Here, the sensitivity was calculated as the percentage of the predicted outputs over the total actual inputs of the corresponding hand sign. We then investigated the recognition rate according to the number of training epochs for hand sign patterns (Fig. 4G). This training and recognition simulation was repeatedly conducted using the LTP/D characteristics of Fig. 3D with respect to the depressing pulse amplitude from −5 to −2 V (see also fig. S6). As shown in the top panel of Fig. 4G, the recognition rate of the ANN increased rapidly as the training continued and was saturated after the 10th training epoch in all pulse amplitude cases. The highest recognition rate was obtained in the case of a −2 V depressing pulse amplitude (optimum pulse condition); in particular, its maximum value reached 99.4% (bottom panel of Fig. 4G). Such a high recognition rate was possible because the softmax function, which amplifies small differences between the input patterns by using an exponential term and distinguishing between the difference clearly, was adopted. Figure S12 presents the results of the recognition rate with respect to the bending radius and the bending cycle; these results indicate an excellent recognition rate exceeding 90%, even under physical bending conditions. For reference, based on the recognition tasks, the required device specification was estimated as follows: For achieving a recognition rate greater than 90%, AS below 5.0 and G_{max}/G_{min} above 10 are required. As shown in table S2, we additionally performed pattern recognition tasks by using the NeuroSim + MLP simulator (*56*) and compared the proposed synaptic device with other previously reported devices in terms of the recognition rates for the Modified National Institute of Standards and Technology dataset. Those results clearly demonstrate the feasibility of the sensory-neuromorphic system concept for sign language translation.

DISCUSSION

In this study, we successfully implemented a flexible artificial synapse on a SIZO/ion gel hybrid structure directly fabricated on a flexible PI substrate, in which the channel conductance was effectively modulated by ion movement in the ion gel. This was possible

because of the low-temperature deposition process of the SIZO channel layer (<150°C) and the improvement of the surface roughness by the PVP buffer layer (12.29→1.81 nm after inserting a 3 wt % PVP layer). Our flexible synaptic device exhibited excellent mechanical flexibility and durability, where the static and dynamic characteristics were maintained stably when bending with a radius of 5 mm and even after 1500 bending cycles. Moreover, its LTP/D characteristics, such as G_{max}/G_{min} and AS, which were optimized by the V_{WC} pulse adjustment, were sustained without any degradation even after the application of 10^4 V_{WC} pulses. Last, we proposed a novel concept of a sensory-neuromorphic system for sign language translation consisting of stretchable-resistive sensors and flexible artificial synapses, which could provide direct and real-time sign language translation to deaf people. The feasibility of the proposed system was confirmed via the training and recognition simulation using the hand sign patterns obtained by the stretchable sensors, and a maximum recognition rate of 99.4% was achieved using the optimized LTP/D characteristics. Moreover, an excellent recognition rate exceeding 90%, even under physical bending conditions, was demonstrated. We expect that this result will become an important basis of research on flexible artificial synapses for future wearable sensory-neuromorphic systems.

MATERIALS AND METHODS

Formation of the SIZO channel layer

A SIZO thin film with an approximate thickness of 30 nm was deposited as the active channel layer with a shadow mask in a radio frequency magnetron sputtering system. The SIZO ceramic target was prepared using high-purity (99.99%) powder mixtures of SiO_2, In_3O_2, and ZnO. Si was incorporated into the IZO (In:Zn = 7:3) system at 1 wt %. During the deposition process, the sputtering power, deposition pressure, and Ar flow rate were 40 W, 4 mtorr, and 40 standard cubic centimeter per minute (sccm), respectively. After the deposition, the SIZO thin films were annealed at 150°C for 2 hours in a furnace.

Fabrication of the flexible SIZO/ion gel synaptic device

The PVP solution was prepared by dissolving PVP powder in propylene glycol methyl ether acetate (Sigma-Aldrich). Next, the PVP solution was spin coated onto a PI film with a size of 2 × 2 cm^2 at 4000 revolutions per minute using a spin coater (ACE 200). The PVP-coated substrate was annealed on a hot plate at 100°C for 10 min and at 200°C for 2 min and 30 s. To form the T_{pre}, T_{post}, and T_{WC}, the first shadow mask was used on the PVP-coated PI substrate, followed by the deposition of 5-nm-thick Ti and 20-nm-thick Au using an electron beam evaporator. The SIZO active channel layer was deposited between T_{pre} and T_{post} with the second shadow mask. The distance between the two terminals and the width of the terminals were 30 and 30 μm, respectively. Then, the ion gel was patterned by exposing it to ultraviolet light for 40 s through the third shadow mask.

Characterization of SIZO/ion gel synaptic device

The OM images of the SIZO/ion gel synaptic devices were obtained using an upright metallurgical microscope (Olympus BX53M). For surface analysis of the synaptic device, AFM measurements were performed at room temperature under ambient conditions using a platinum/iridium–coated Si tip in an NX10 system (Park Systems Corp.). The $RMS_{roughness}$ value was calculated using the following equation

$$RMS_{roughness} = \sqrt{\frac{1}{A}\iint_A Z^2(x,y)\,dx\;dy}$$

For analysis of the I_{post}-V_{WC} and LTP/D characteristics of the SIZO/ion gel synaptic devices, electrical measurements were conducted at 20°C and a relative humidity of 40% (monitored by a commercial thermo-hygrometer) using a Keysight B2901A parameter analyzer. To avoid the measurement errors appearing below the minimum source current resolution of 10^{-12} A, all the synaptic characteristics, including V_{th}, G_{post}, and G_{max}/G_{min}, were extracted from the raw I-V data above 10^{-10} A.

Fabrication of the CNT/SEBS stretchable sensor

A polystyrene-block-poly(ethylene-ran-butylene)-block-polystyrene (SEBS) H1062 elastomer (Asahi Kasei Company) substrate was prepared, where SEBS H1062 (200 mg/ml in toluene; Sigma-Aldrich) was cast onto a petri dish to form elastic films with an approximate thickness of 0.2 mm. CNTs (U.S. Research Nanomaterial) dispersed in 10 ml of toluene at a concentration of 1.5 wt % were then ultrasonicated for 30 min. The CNT solution was coated on the SEBS substrate, and the toluene was evaporated in a fume hood to embed the resistive sensing material onto the substrate.

Weight update in the synaptic device for pattern recognition tasks

To update the synaptic weight ($W_{n,m}$), the sgn(ΔW) was calculated by subtracting the output value to the corresponding label value [i.e., sgn(ΔW) = $k_m - O_m$]. If sgn(ΔW) is positive (positive feedback), then $G_{n,m}{}^+$ increases and, simultaneously, $G_{n,m}{}^-$ decreases, causing the potentiation of the synaptic ($W_{n,m}\uparrow = G_{n,m}{}^+\uparrow - G_{n,m}{}^-\downarrow$). In contrast, if sgn($\Delta W$) is negative (negative feedback), then the synaptic weight is depressed ($W_{n,m}\downarrow = G_{n,m}{}^+\downarrow - G_{n,m}{}^-\uparrow$). If sgn($\Delta W$) was zero, then the synaptic weight was not updated. All weight values in the synaptic weight matrix were updated according to the determined sgn(ΔW). Here, the conductance change (ΔG) was determined using the following equations

$$G_{n+1} = G_n + \Delta G_P = G_n + \alpha_P e^{-NL_P\frac{G_n - G_{min}}{G_{max} - G_{min}}} (\Delta G > 0, G\uparrow),$$
$$G_{n+1} = G_n + \Delta G_D = G_n - \alpha_D e^{NL_D\frac{G_{max} - G_n}{G_{max} - G_{min}}} (\Delta G < 0, G\downarrow)$$

In these equations, G_{n+1} and G_n denote the synaptic conductance when the n + 1th and nth pulses are applied, respectively, and parameters α and NL denote the amount of conductance change and the nonlinearity, respectively. Details regarding the estimation of the α and NL values are provided in fig. S13.

Hand sign language translating simulation in sensory-neuromorphic system

The hand sign language translating simulation was conducted on the basis of a single-layer perceptron (SLP) ANN, where the ANN had a size of 15 × 8 and was theoretically constructed using nonideal factors, such as G_{max}/G_{min} and AS. The input voltage values for the hand sign patterns were normalized to 256 grayscale values from 0 to 1 V, and the softmax function was used as the activation function. After training the SLP ANN with 60,000 patterns (one training epoch), the recognition tasks for the 10,000 separate testing patterns were performed. The recognition rate was calculated at every 60,000th training step during the training process.

SUPPLEMENTERY MATERIALS

Supplementary material for this article is available at https://science.org/doi/10.1126/sciadv.abg9450

REFERENCES AND NOTES

1. Y. Lee, J. Park, A. Choe, S. Cho, J. Kim, H. Ko, Mimicking human and biological skins for multifunctional skin electronics. *Adv. Funct. Mater.* **30**, 1904523 (2020).
2. Y. Song, J. Min, Y. Yu, H. Wang, Y. Yang, H. Zhang, W. Gao, Wireless battery-free wearable sweat sensor powered by human motion. *Sci. Adv.* **6**, 10.1126/sciadv.aay9842, (2020).
3. Z. Zhang, T. He, M. Zhu, Z. Sun, Q. Shi, J. Zhu, B. Dong, M. R. Yuce, C. Lee, Deep learning-enabled triboelectric smart socks for IoT-based gait analysis and VR applications. *npj Flex. Electron.* **4**, 29 (2020).
4. J. Kim, A. S. Campbell, B. E. F. de Ávila, J. Wang, Wearable biosensors for healthcare monitoring. *Nat. Biotechnol.* **37**, 389–406 (2019).
5. S. Lee, S. Gandla, M. Naqi, U. Jung, H. Youn, D. Pyun, Y. Rhee, S. Kang, H. J. Kwon, H. Kim, M. G. Lee, S. Kim, All-day mobile healthcare monitoring system based on heterogeneous stretchable sensors for medical emergency. *IEEE Trans. Ind. Electron.* **67**, 8808–8816 (2020).
6. S. Gandla, M. Naqi, M. Lee, J. J. Lee, Y. Won, P. Pujar, J. Kim, S. Lee, S. Kim, Highly linear and stable flexible temperature sensors based on laser-induced carbonization of polyimide substrates for personal mobile monitoring. *Adv. Mater. Technol.* **5**, 2000014 (2020).
7. H. Joo, Y. Lee, J. Kim, J. S. Yoo, S. Yoo, S. Kim, A. K. Arya, S. Kim, S. H. Choi, N. Lu, H. S. Lee, S. Kim, S. T. Lee, D. H. Kim, Soft implantable drug delivery device integrated wirelessly with wearable devices to treat fatal seizures. *Sci. Adv.* **7**, 10.1126/sciadv.abd4639, (2021).
8. W. Xu, S.-Y. Min, H. Hwang, T.-W. Lee, Organic core-sheath nanowire artificial synapses with femtojoule energy consumption. *Sci. Adv.* **2**, e1501326 (2016).
9. Y. Fu, L. A. Kong, Y. Chen, J. Wang, C. Qian, Y. Yuan, J. Sun, Y. Gao, Q. Wan, Flexible neuromorphic architectures based on self-supported multiterminal organic transistors. *ACS Appl. Mater. Interfaces* **10**, 26443–26450 (2018).
10. J. W. Borchert, U. Zschieschang, F. Letzkus, M. Giorgio, R. T. Weitz, M. Caironi, J. N. Burghartz, S. Ludwigs, H. Klauk, Flexible low-voltage high-frequency organic thin-film transistors. *Sci. Adv.* **6**, 10.1126/sciadv.aaz5156, (2020).
11. L. Gao, Flexible device applications of 2D semiconductors. *Small* **13**, 1603994 (2017).
12. H. Park, D. S. Oh, K. J. Lee, D. Y. Jung, S. Lee, S. Yoo, S. Y. Choi, Flexible and transparent thin-film transistors based on two-dimensional materials for active-matrix display. *ACS Appl. Mater. Interfaces* **12**, 4749–4754 (2020).
13. H. Tan, Q. Tao, I. Pande, S. Majumdar, F. Liu, Y. Zhou, P. O. Å. Persson, J. Rosen, S. van Dijken, Tactile sensory coding and learning with bio-inspired optoelectronic spiking afferent nerves. *Nat. Commun.* **11**, 1369 (2020).
14. K. T. Kim, S. H. Kang, J. Kim, J. S. Heo, Y. H. Kim, S. K. Park, An ultra-flexible solution-processed metal-oxide/carbon nanotube complementary circuit amplifier with highly reliable electrical and mechanical stability. *Adv. Electron. Mater.* **6**, 1900845 (2020).
15. J. Kim, S. Kwon, Y. K. Kang, Y. Kim, M. Lee, K. Han, A. Facchetti, M. Kim, S. K. Park, A skin-like two-dimensionally pixelized full-color quantum dot photodetector. *Sci. Adv.* **5**, 10.1126/sciadv.aax8801, (2019).
16. B. Wang, A. Thukral, Z. Xie, L. Liu, X. Zhang, W. Huang, X. Yu, C. Yu, T. J. Marks, A. Facchetti, Flexible and stretchable metal oxide nanofiber networks for multimodal and monolithically integrated wearable electronics. *Nat. Commun.* **11**, 10.1126/sciadv.aax8801, (2020).
17. K. Nomura, H. Ohta, A. Takagi, T. Kamiya, M. Hirano, H. Hosono, Room-temperature fabrication of transparent flexible thin-film transistors using amorphous oxide semiconductors. *Nature* **432**, 488–492 (2004).
18. P. Grey, D. Gaspar, I. Cunha, R. Barras, J. T. Carvalho, J. R. Ribas, E. Fortunato, R. Martins, L. Pereira, Handwritten oxide electronics on paper. *Adv. Mater. Technol.* **2**, 2–8 (2017).
19. J. Y. Choi, S. Kim, B.-U. Hwang, N.-E. Lee, S. Y. Lee, Flexible SiInZnO thin film transistor with organic/inorganic hybrid gate dielectric processed at 150°C. *Semicond. Sci. Technol.* **31**, 12507 (2016).
20. K. Sim, Z. Rao, Z. Zou, F. Ershad, J. Lei, A. Thukral, J. Chen, Q. A. Huang, J. Xiao, C. Yu, Metal oxide semiconductor nanomembrane–based soft unnoticeable multifunctional electronics for wearable human-machine interfaces. *Sci. Adv.* **5**, 1–11 (2019).
21. M. Zulqarnain, S. Stanzione, G. Rathinavel, S. Smout, M. Willegems, K. Myny, E. Cantatore, A flexible ECG patch compatible with NFC RF communication. *npj Flex. Electron.* **4**, 13 (2020).
22. K. Yang, S. Yuan, Y. Huan, J. Wang, L. Tu, J. Xu, Z. Zou, Y. Zhan, L. Zheng, F. Seoane, Tunable flexible artificial synapses: A new path toward a wearable electronic system. *npj Flex. Electron.* **2**, 20 (2018).
23. Y. Lee, J. Y. Oh, W. Xu, O. Kim, T. R. Kim, J. Kang, Y. Kim, D. Son, J. B. H. Tok, M. J. Park, Z. Bao, T. W. Lee, Stretchable organic optoelectronic sensorimotor synapse. *Sci. Adv.* **4**, 10.1126/sciadv.aat7387, (2018).
24. D. Choi, M. K. Song, T. Sung, S. Jang, J. Y. Kwon, Energy scavenging artificial nervous system for detecting rotational movement. *Nano Energy* **74**, 104912 (2020).
25. Y. R. Lee, T. Q. Trung, B. U. Hwang, N. E. Lee, A flexible artificial intrinsic-synaptic tactile sensory organ. *Nat. Commun.* **11**, 2753 (2020).
26. H. Shim, K. Sim, F. Ershad, P. Yang, A. Thukral, Z. Rao, H. J. Kim, Y. Liu, X. Wang, G. Gu, L. Gao, X. Wang, Y. Chai, C. Yu, Stretchable elastic synaptic transistors for neurologically integrated soft engineering systems. *Sci. Adv.* **5**, 10.1126/sciadv.aax4961, (2019).
27. S. Ham, M. Kang, S. Jang, J. Jang, S. Choi, T. W. Kim, G. Wang, One-dimensional organic artificial multi-synapses enabling electronic textile neural network for wearable neuromorphic applications. *Sci. Adv.* **6**, 10.1126/sciadv.aba1178, (2020).
28. Y. Y. Zhao, W. J. Sun, J. Wang, J. H. He, H. Li, Q. F. Xu, N. J. Li, D. Y. Chen, J. M. Lu, All-inorganic ionic polymer-based memristor for high-performance and flexible artificial synapse. *Adv. Funct. Mater.* **30**, 1–8 (2020).
29. D. W. Kim, J. C. Yang, S. Lee, S. Park, Neuromorphic processing of pressure signal using integrated sensor-synaptic device capable of selective and reversible short- and long-term plasticity operation. *ACS Appl. Mater. Interfaces* **12**, 23207–23216 (2020).
30. C. Wan, P. Cai, X. Guo, M. Wang, N. Matsuhisa, L. Yang, Z. Lv, Y. Luo, X. J. Loh, X. Chen, An artificial sensory neuron with visual-haptic fusion. *Nat. Commun.* **11**, 4602 (2020).
31. Y. Zang, H. Shen, D. Huang, C. A. Di, D. Zhu, A dual-organic-transistor-based tactile-perception system with signal-processing functionality. *Adv. Mater.* **29**, 1606088 (2017).
32. Y. Kim, A. Chortos, W. Xu, Y. Liu, J. Y. Oh, D. Son, J. Kang, A. M. Foudeh, C. Zhu, Y. Lee, S. Niu, J. Liu, R. Pfattner, Z. Bao, T. W. Lee, A bioinspired flexible organic artificial afferent nerve. *Science* **360**, 998–1003 (2018).
33. S. Kim, Y. Lee, H.-D. Kim, S.-J. Choi, A tactile sensor system with sensory neurons and a perceptual synaptic network based on semivolatile carbon nanotube transistors. *NPG Asia Mater.* **12**, 76 (2020).
34. W. G. Regehr, L. F. Abbott, Synaptic computation. *Nature* **431**, 796–803 (2004).
35. A. Richter, J. J. BelBruno, Characterization of functional states in nicotine- and cotinine-imprinted poly(4-vinylphenol) films by nanoindentation. *J. Appl. Polym. Sci.* **124**, 2798–2806 (2012).
36. S. Kim, M. Lim, Y. Kim, H. D. Kim, S. J. Choi, Impact of synaptic device variations on pattern recognition accuracy in a hardware neural network. *Sci. Rep.* **8**, 2638 (2018).
37. J. Sun, S. Oh, Y. Choi, S. Seo, M. J. Oh, M. Lee, W. B. Lee, P. J. Yoo, J. H. Cho, J. H. Park, Optoelectronic synapse based on IGZO-alkylated graphene oxide hybrid structure. *Adv. Funct. Mater.* **28**, 1804397 (2018).
38. S. Seo, J.-J. Lee, H.-J. Lee, H. W. Lee, S. Oh, J. J. Lee, K. Heo, J.-H. Park, Recent progress in artificial synapses based on two-dimensional van der waals materials for brain-inspired computing. *ACS Appl. Electron. Mater.* **2**, 371–388 (2020).
39. S. Seo, B. S. Kang, J. J. Lee, H. J. Ryu, S. Kim, H. Kim, S. Oh, J. Shim, K. Heo, S. Oh, J. H. Park, Artificial van der waals hybrid synapse and its application to acoustic pattern recognition. *Nat. Commun.* **11**, 3936 (2020).
40. S. Oh, S. Jung, M. H. Ali, J. H. Kim, H. Kim, J. H. Park, Highly stable artificial synapse consisting of low-surface defect van der waals and self-assembled materials. *ACS Appl. Mater. Interfaces* **12**, 38299–38305 (2020).
41. Y. Choi, S. Oh, C. Qian, J. H. Park, J. H. Cho, Vertical organic synapse expandable to 3D crossbar array. *Nat. Commun.* **11**, 4595 (2020).
42. J. Huang, J. Chen, R. Yu, Y. Zhou, Q. Yang, E. Li, Q. Chen, H. Chen, T. Guo, Tuning the synaptic behaviors of biocompatible synaptic transistor through ion-doping. *Org. Electron.* **89**, 106019 (2021).
43. T. S. Kim, Y. Lee, W. Xu, Y. H. Kim, M. Kim, S. Y. Min, T. H. Kim, H. W. Jang, T. W. Lee, Direct-printed nanoscale metal-oxide-wire electronics. *Nano Energy* **58**, 437–446 (2019).
44. H. L. Park, Y. Lee, N. Kim, D. G. Seo, G. T. Go, T. W. Lee, Flexible neuromorphic electronics for computing, soft robotics, and neuroprosthetics. *Adv. Mater.* **32**, 1903558 (2020).
45. S. Yang, J. Y. Bak, S. M. Yoon, M. K. Ryu, H. Oh, C. S. Hwang, G. H. Kim, S. H. K. Park, J. Jang, Low-temperature processed flexible In-Ga-Zn-O thin-film transistors exhibiting high electrical performance. *IEEE Electron Device Lett.* **32**, 1692–1694 (2011).
46. B. J. Kim, H. Jang, S. K. Lee, B. H. Hong, J. H. Ahn, J. H. Cho, High-performance flexible graphene field effect transistors with ion gel gate dielectrics. *Nano Lett.* **10**, 3464–3466 (2010).
47. J. Pu, Y. Yomogida, K. Liu, L. Li, Y. Iwasa, T. Takenobu, Highly flexible MoS_2 thin-film transistors with ion gel dielectrics. *Nano Lett.* **13**, 10–14 (2012).
48. S. Yu, Neuro-inspired computing with emerging nonvolatile memorys. *Proc. IEEE* **106**, 260–285 (2018).
49. Z. Zhou, K. Chen, X. Li, S. Zhang, Y. Wu, Y. Zhou, K. Meng, C. Sun, Q. He, W. Fan, E. Fan, Z. Lin, X. Tan, W. Deng, J. Yang, J. Chen, Sign-to-speech translation using machine-learning-assisted stretchable sensor arrays. *Nat. Electron.* **3**, 571–578 (2020).
50. F. Zhou, Y. Chai, Near-sensor and in-sensor computing. *Nat. Electron.* **3**, 664–671 (2020).
51. Y. Wu, Y. Liu, Y. Zhou, Q. Man, C. Hu, W. Asghar, F. Li, Z. Yu, J. Shang, G. Liu, M. Liao, R. W. Li, A skin-inspired tactile sensor for smart prosthetics. *Sci. Robot.* **3**, 10.1126/scirobotics.aat0429, (2018).
52. C. Zhang, W. Bin Ye, K. Zhou, H. Y. Chen, J. Q. Yang, G. Ding, X. Chen, Y. Zhou, L. Zhou, F. Li, S. T. Han, Bioinspired artificial sensory nerve based on nafion memristor. *Adv. Funct. Mater.* **29**, 1808783 (2019).

53. Y. Liu, W. Yang, Y. Yan, X. Wu, X. Wang, Y. Zhou, Y. Hu, H. Chen, T. Guo, Self-powered high-sensitivity sensory memory actuated by triboelectric sensory receptor for real-time neuromorphic computing. *Nano Energy* **75**, 104930 (2020).
54. L. Wang, Y. Liu, Q. Liu, Y. Zhu, H. Wang, Z. Xie, X. Yu, Y. Zi, A metal-electrode-free, fully integrated, soft triboelectric sensor array for self-powered tactile sensing. *Microsyst. Nanoeng.* **6**, 59 (2020).
55. C. Qian, S. Oh, Y. Choi, S. Seo, J. Sun, J. H. Park, J. H. Cho, Rational band engineering of an organic double heterojunction for artificial synaptic devices with enhanced state retention and linear update of synaptic weight. *ACS Appl. Mater. Interfaces* **12**, 10737–10745 (2020).
56. Y. Luo, X. Peng, S. Yu, MLP+NeuroSimV3.0: Improving on-chip learning performance with device to algorithm optimizations, in *Proceedings of the International Conference on Neuromorphic Systems (ICONS'19)*, ACM, Knoxvillw, Tennessee, USA, 2019.
57. C. Sen Yang, D. S. Shang, N. Liu, E. J. Fuller, S. Agrawal, A. A. Talin, Y. Q. Li, B. G. Shen, Y. Sun, All-solid-state synaptic transistor with ultralow conductance for neuromorphic computing. *Adv. Funct. Mater.* **28**, 1804170 (2018).
58. L. Yin, C. Han, Q. Zhang, Z. Ni, S. Zhao, K. Wang, D. Li, M. Xu, H. Wu, X. Pi, D. Yang, Synaptic silicon-nanocrystal phototransistors for neuromorphic computing. *Nano Energy* **63**, 103859 (2019).
59. P. Y. Chen, X. Peng, S. Yu, Neurosim+: An integrated device-to-algorithm framework for benchmarking synaptic devices and array architectures, in *Proceedings of the 2017 IEEE International Electron Devices Meeting (IEDM)*, 2017.
60. C. Qian, S. Oh, Y. Choi, J. H. Kim, J. Sun, H. Huang, J. Yang, Y. Gao, J. H. Park, J. H. Cho, Solar-stimulated optoelectronic synapse based on organic heterojunction with linearly potentiated synaptic weight for neuromorphic computing. *Nano Energy* **66**, 104095 (2019).
61. J. Y. Gerasimov, R. Gabrielsson, R. Forchheimer, E. Stavrinidou, D. T. Simon, M. Berggren, S. Fabiano, An evolvable organic electrochemical transistor for neuromorphic applications. *Adv. Sci.* **6**, 1801339 (2019).
62. H. Ling, N. Wang, A. Yang, Y. Liu, J. Song, F. Yan, Dynamically reconfigurable short-term synapse with millivolt stimulus resolution based on organic electrochemical transistors. *Adv. Mater. Technol.* **4**, 1900471 (2019).
63. S. Ginnaram, S. Maikap, Memristive and artificial synapse performance by using TiO_x/Al_2O_3 interface engineering in MoS_2-based metallic filament memory. *J. Phys. Chem. Solid* **151**, 109901 (2021).
64. L. Q. Zhu, C. J. Wan, P. Q. Gao, Y. H. Liu, H. Xiao, J. C. Ye, Q. Wan, Flexible proton-gated oxide synaptic transistors on Si membrane. *ACS Appl. Mater. Interfaces* **8**, 21770–21775 (2016).
65. F. Yu, L. Q. Zhu, W. T. Gao, Y. M. Fu, H. Xiao, J. Tao, J. M. Zhou, Chitosan-based polysaccharide-gated flexible indium tin oxide synaptic transistor with learning abilities. *ACS Appl. Mater. Interfaces* **10**, 16881–16886 (2018).
66. T. Y. Long, L. Q. Zhu, Y. B. Guo, Z. Y. Ren, H. Xiao, Z. Y. Ge, L. Wang, Flexible oxide neuromorphic transistors with synaptic learning functions. *J. Phys. D. Appl. Phys.* **52**, 405101 (2019).
67. S. Park, J. T. Jang, S. J. Choi, D. M. Kim, D. H. Kim, Synaptic behavior of flexible IGZO TFTs with Al_2O_3 gate insulator by low temperature ALD. *Proc. IEEE Conf. Nanotechnol.* **2019**, 517–520 (2019).
68. G. Zhong, M. Zi, C. Ren, Q. Xiao, M. Tang, L. Wei, F. An, S. Xie, J. Wang, X. Zhong, M. Huang, J. Li, Flexible electronic synapse enabled by ferroelectric field effect transistor for robust neuromorphic computing. *Appl. Phys. Lett.* **117**, 092903 (2020).
69. H. Wei, Y. Ni, L. Sun, H. Yu, J. Gong, Y. Du, M. Ma, H. Han, W. Xu, Flexible electro-optical neuromorphic transistors with tunable synaptic plasticity and nociceptive behavior. *Nano Energy* **81**, 105648 (2021).
70. S. H. Jo, T. Chang, I. Ebong, B. B. Bhadviya, P. Mazumder, W. Lu, Nanoscale memristor device as synapse in neuromorphic systems. *Nano Lett.* **10**, 1297–1301 (2010).
71. W. Wu, H. Wu, B. Gao, P. Yao, X. Zhang, X. Peng, S. Yu, H. Qian, A methodology to improve linearity of analog RRAM for neuromorphic computing. *Dig. Tech. Pap. Symp. VLSI Technol.* **2018**, 103–104 (2018).
72. S. Park, A. Sheri, J. Kim, J. Noh, J. Jang, M. Jeon, B. Lee, B. R. Lee, B. H. Lee, H. Hwang, Neuromorphic speech systems using advanced ReRAM-based synapse. *Tech. Dig. Int. Electron Devices Meet. IEDM* **2013**, 625–628 (2013).
73. J. Woo, K. Moon, J. Song, S. Lee, M. Kwak, J. Park, H. Hwang, Improved synaptic behavior under identical pulses using AlO_x/HfO_2 bilayer RRAM array for neuromorphic systems. *IEEE Electron Device Lett.* **37**, 994–997 (2016).
74. D. Kuzum, R. G. D. Jeyasingh, B. Lee, H. P. Wong, Nanoelectronic programmable synapses based on phase change materials for brain-inspired computing. *Nano Lett.* **12**, 2179–2186 (2012).
75. S. Choi, S. H. Tan, Z. Li, Y. Kim, C. Choi, P. Y. Chen, H. Yeon, S. Yu, J. Kim, SiGe epitaxial memory for neuromorphic computing with reproducible high performance based on engineered dislocations. *Nat. Mater.* **17**, 335–340 (2018).
76. M. Jerry, P. Y. Chen, J. Zhang, P. Sharma, K. Ni, S. Yu, S. Datta, Ferroelectric FET Analog synapse for acceleration of deep neural network training, in *Proceedings of the 2017 IEEE International Electron Devices Meeting (IEDM)*, San Francisco, USA, 2 to 6 December 2017.

Acknowledgments

Funding: This research was supported by the Basic Science Research Program, Basic Research Laboratory Program, and Nano-Material Technology Development Program through National Research Foundation of Korea (NRF) grants funded by the Korean government (MSIP) (2020R1A4A200280612, 2019M3F3A1A0107445113, 2020M3F3A2A0208247312, and 2021R1A2C201002611), and the Future Semiconductor Device Technology Development Program (10067739) funded by the Ministry of Trade, Industry and Energy (MOTIE), and the Korean Semiconductor Research Consortium (KSRC). This work was also supported by Samsung Electronics Co. Ltd. (IO201210-07994-01). **Author contributions:** S.O., J.-I.C., B.H.L., and J.-H.P. designed the experiments and analyzed the data. J.-H.P. supervised the study. All authors discussed the results and contributed to the manuscript. **Competing interests:** The authors declare that they have no competing interests. **Data and materials availability:** All data needed to evaluate the conclusions in the paper are present in the paper and/or the Supplementary Materials.

Submitted 5 February 2021
Accepted 9 September 2021
Published 29 October 2021
10.1126/sciadv.abg9450

Citation: S. Oh, J.-I. Cho, B. H. Lee, S. Seo, J.-H. Lee, H. Choo, K. Heo, S. Y. Lee, J.-H. Park, Flexible artificial Si-In-Zn-O/ion gel synapse and its application to sensory-neuromorphic system for sign language translation. *Sci. Adv.* **7**, eabg9450 (2021).